applied sciences

MDPI

Article

Investigation of Load Characteristics and Stress-Energy Evolution Laws of Gob-Side Roadways Under Thick and Hard Roofs

Jinlong Zhou [1,2,3,*], Junfeng Pan [2], Yongxue Xia [2], Wengang Liu [4], Taotao Du [2] and Jianhong Wu [2]

1 Coal Mining Branch, China Coal Research Institute, Beijing 100013, China
2 Coal Mining Research Institute, China Coal Technology and Engineering Group, Beijing 100013, China; panjunfeng@yeah.net (J.P.)
3 School of Energy and Mining Engineering, China University of Mining and Technology (Beijing), Beijing 100083, China
4 Research Institute of Emergency Science, China Coal Research Institute, Beijing 100013, China; liuwgccteg@126.com
* Correspondence: zhoujlcumtb@163.com

Abstract: The stress environments of gob-side roadways (GSRs) are becoming increasingly complex during deep coal mining under thick and hard roofs. This leads to strong strata behaviors, including roadway floor heave, roof subsidence, and even coal bursts. Among them, coal bursts pose the greatest threat to production safety in coal mines. Coal bursts in a GSR strongly correlate with the load characteristics and stress-energy evolution laws of the roadway. This study analyzes the roof structures of double working faces (DWFs) during the initial weighting stage (IWS) and full mining stage (FMS) of gob-side working faces (GSWFs). This study also explores how varying roof structures affect the stability of GSRs. Three-dimensional roof structure models of DWFs and mechanical models of dynamic and static loads superposition on a GSR throughout the IWS and FMS of a GSWF were developed. An analysis identified the primary stress sources affecting the GSR throughout various mining stages of the GSWF. Subsequently, the principle of "three-load" superposition was developed. A novel method was proposed to quantify the stress state in the GSR surrounding rock across different mining stages of the GSWF. The method quantitatively characterizes the load of the GSR surrounding rock. Based on this, the criterion for judging the burst failure of the roadway was established. Numerical simulations are used to analyze the stress-energy evolution laws of the working face, coal pillar, and GSR surrounding rock during the mining process of the GSWF. These findings offer valuable references for studying and preventing coal bursts in GSRs under equivalent geological situations.

Keywords: deep coal mining; thick and hard roofs; gob-side roadways; load characteristics; stress-energy evolution laws

check for updates

Citation: Zhou, J.; Pan, J.; Xia, Y.; Liu, W.; Du, T.; Wu, J. Investigation of Load Characteristics and Stress-Energy Evolution Laws of Gob-Side Roadways Under Thick and Hard Roofs. *Appl. Sci.* **2024**, *14*, 9513. https://doi.org/10.3390/app14209513

Academic Editor: Nikolaos Koukouzas

Received: 12 September 2024
Revised: 15 October 2024
Accepted: 17 October 2024
Published: 18 October 2024

1. Introduction

Recently, some coal mines in Ordos region of China have reached depths of 600–750 m [1]. These deep coal mines feature high and wide working faces overlaid by multiple thick and hard roofs. Combining deep and high-intensity mining subjects the stope to complex stress conditions. Coal bursts frequently occur in the gob-side roadway (GSR) preceding the working face throughout the extraction of the gob-side working face (GSWF). Such occurrences present substantial hazards to the workforce engaged in underground operations. Coal bursts in GSRs are strongly influenced by the roof structure of double working faces (DWFs) under thick and hard roofs and their loading effect on the GSR. Mining-induced stress and energy evolution play a crucial role in coal burst occurrences at GSRs. To elucidate the mechanism of coal bursts in GSRs and develop effective prevention strategies, it is crucial to investigate the roof structure of DWFs and the stress-energy evolution laws and load characteristics of GSRs during the mining process of GSWFs.

Coal extraction induces fracturing and movement in the overlying strata, forming different overburden spatial structures. These overburden structures and their mechanical properties significantly influence the strata behavior in stopes [2–5]. Extensive research has focused on characterizing the overburden structure of working faces. Early research primarily originated from German, Soviet, and Belgian scholars. Their work introduced several hypotheses, including the "cantilever beam" [6], "pressure arch" [7], "hinging rock strata", and "pre-formed fissure" hypotheses. On this basis, Chinese scholars have conducted relevant research: Qian [8,9] put forward the "voussoir beam" theory and advanced the field by introducing the key strata theory, expanding on the "voussoir beam" theory [10]. Song [11] proposed the "transfer rock beam" theory, explaining stress distribution in mining-affected areas. Over the past 15 years, researchers have developed numerous roof structure models for different mining conditions based on these foundational theories. He [12–14] proposed the "cutting cantilever beam" theory, which paved the way for the cutting roof and stress relief technology. This innovation enables the creation of roadways without coal pillars through automated means. This advancement holds particular importance for roadway surrounding rock control and coal burst prevention. Dou et al. [15] proposed an overburden spatial structure model for single, double, and island working face mining boundary conditions, denoted as "O-X, F, and T" structures, respectively. They validated this model using microseismic monitoring techniques, providing empirical support for their theoretical framework. Huang et al. [16] proposed a structure model for main roofs due to insufficient gob filling in large mining height working faces. Yu et al. [17,18] modelled overburden in the large-space stopes of extremely thick coal seam mining, identifying distinct near-field and far-field key strata responses. Zuo et al. [19–21] proposed an "analogous hyperbola (hyperboloid)" theoretical model for overburden movement. This model integrates the mechanical analysis of breaking patterns in different strata and similar simulation experiments. These studies have significantly enriched ground control theory in coal mining.

Coal bursts in the roadway strongly correlate with the stress induced by mining operations and the energy evolution within the roadway surrounding rock [22–26]. Scholars have conducted extensive research grounded in theoretical modelling, physical experiments, numerical computations, and in situ measurements, laying the groundwork for analyzing the stability of roadway surrounding rock. Zhang et al. [27] measured the lateral abutment pressure distribution within coal pillars and, based on this, proposed a mechanical model validated through numerical simulation. To establish roof fracture criteria, Bai et al. [28] developed a dynamic roof structure model through monitoring, analysis, and simulation. Zhang et al. [29] examined the stress evolution properties of GSRs through numerical simulation. They elucidated the load transfer mechanism of the surrounding rock and developed a model for it. Lou et al. [30] conducted large-scale physical similar simulation experiments to study mining-induced stress evolution. Their results revealed an arch-shaped distribution for principal stress with high stress concentrations at the arch shoulders and varying vertical stress patterns in different areas. Wang et al. [31,32] conducted computational modelling analysis regarding the rotation characteristics of stress in deep mining. They proposed and field-tested a method to improve roof stability by controlling stress rotation. Ma et al. [33] highlighted that the abrupt discharge of accumulated energy is the leading cause of coal bursts. The intensity of coal bursts correlates closely with the degree of energy accumulation.

Previous research has focused on the roof structures of the working face and their mechanical analysis, examining the patterns of stress redistribution and energy accumulation in the roadway surrounding rock. However, few studies have quantitatively examined the relationship between roof structures and loads on GSRs at the initial weighting stage (IWS) and full mining stage (FMS) of GSWFs. This problem is particularly evident in thick and hard roofs in the Ordos region. The mechanism by which different roof structures load the

GSR surrounding rock remains to be determined. Coal bursts in GSRs are closely linked to roof structure morphology and its loading effect on roadway surrounding rock. Addressing this problem, we develop roof structure models of DWFs for various stages of GSWFs and analyze the load sources of the GSR surrounding rock. A stress calculation method for the roadway surrounding rock is proposed which can quantitatively evaluate the load patterns in the roadway surrounding rock. Concurrently, we analyze the distribution of stress and energy in roadway surrounding rock through numerical simulation. This study provides a valuable framework to understand the underlying mechanisms and mitigate the risk of coal bursts in GSRs.

2. Engineering Background

A multilayered thick and hard sandstone overburden overlays the working face in some deep coal mines within the Ordos region. The high static and dynamic load combination resulting from thick and hard roofs fracturing has led to frequent coal bursts in GSRs during coal mining. These events present substantial hazards to coal mine operations. This study takes the coal bursts in the GSR throughout the mining process of the 3^{-1}103 working face at Hongqinghe Coal Mine in Xinjie Town, located in Ordos, which serves as the engineering background. Then, this study analyzes the roof structure, load behavior of the GSR, and the distribution of stress and energy induced by the mining of the GSWF. This study aims to provide insights into the mechanisms of coal bursts in GSRs and contribute to developing effective prevention strategies.

The 3^{-1}103 working face, adjacent to the 3^{-1}101 working face gob, measures 210 m in working face length, 2480 m in mining length, and 707.15 m in average depth. The coal seam averages 6.36 m in thickness. A fully mechanized mining method with a large mining height is used for coal mining. The working face comprises three roadways: the 3^{-1}101 material roadway, the 3^{-1}103 belt roadway, and the 3^{-1}103 material roadway. The width of the coal pillars between adjacent roadways is 30 m. The roof and two sides of the roadway are supported by bolts and cables. Notably, coal bursts in the 3^{-1}103 working face primarily occur in the 3^{-1}101 material roadway, also known as the GSR, which is located near the advancing working face. These coal bursts manifest as dynamic phenomena, including instantaneous floor heave, roof subsidence, rib spalling, and broken bolts and cables. Figure 1 illustrates the arrangement of the 3^{-1}101 and 3^{-1}103 working faces and typical bursting failure characteristics of the roadway.

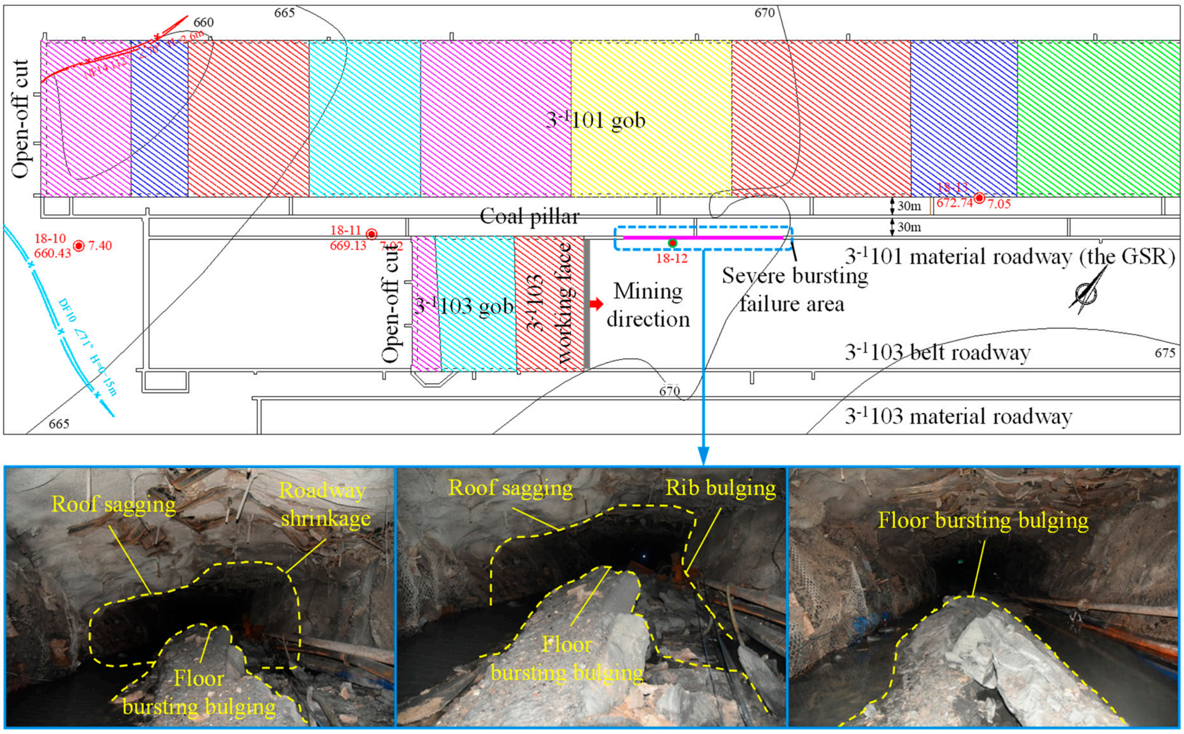

Figure 1. The arrangement of the $3^{-1}101$ and $3^{-1}103$ working faces and the typical bursting failure characteristics of the GSR [34].

Relevant studies have shown that the occurrence of coal bursts in GSRs under thick and hard roofs conditions is significantly influenced by the roof structure of the working face and the stress environment of surrounding rock [1,29,33,35,36]. Building on these findings, this study develops a roof structure model of DWFs for three critical stages during the mining process of GSWFs: the IWS, periodic weighting stage (PWS), and FMS. These models aid in examining the load characteristics of the GSR surrounding rock. A new stress determination method for roadway surrounding rock is developed. Mining-induced stress and energy evolution in the roadway are investigated by numerical simulation. Our objective is to gain insights into coal burst mechanisms in GSRs and inform prevention strategies.

3. Roof Structure of DWFs and GSR Load Analysis

The GSR experiences dynamic and static loads stemming from roof collapse in the gob adjacent to the first working face (FWF) throughout extraction. Subsequently, when mining the GSWF, the GSR is subjected to a more complex stress environment. This environment combines static forces adjacent to the gob with loads from the GSWF, comprising dynamic and static elements. The cumulative effect of two mining stages significantly increases the risk of severe damage to the GSR. Consequently, the likelihood of coal bursts rises substantially. To analyze these complex load characteristics, the roof structure model of DWFs is established for three mining stages: the IWS, PWS, and FMS of the GSWF. By applying this model, we can effectively assess the load characteristics of the GSR during the secondary mining stage.

3.1. Roof Structure and Stress Calculation of Roadway Surrounding Rock During the IWS

According to key strata theory [10], an analysis was conducted on the overlying strata exposed in the drilling histogram of No. 18–12 (Figure 2) near an area prone to coal bursts. Medium-grained sandstone (No. 16) and fine-grained sandstone (No. 15) with high strength and large thickness were classified as inferior key strata I (IKS I) and inferior key strata II (IKS II). The key strata fracture structure significantly influences the stress evolution of the surrounding rock. Accurate assessment of the stress state and the loading patterns on the roadway must be evaluated in relation to the fracture structure of the key strata, therefore enabling the analysis of coal burst mechanisms.

No.	Stratigraphic Column	Thickness /m	Depth /m	Lithology
1		2.70	311.81	Mudstone
2		21.55	333.36	Fine-grained sandstone
3		34.12	367.48	Medium-grained sandstone
4		47.30	414.78	Fine-grained sandstone
5		27.26	442.04	Pebblestone
6		36.65	478.69	Coarse-grained sandstone
7		39.29	517.98	Medium-grained sandstone
8		16.44	534.42	Fine-grained sandstone
9		28.83	563.25	Mudstone
10		15.49	578.74	Sandy mudstone
11		14.47	593.21	Siltstone
12		8.13	601.34	Sandy mudstone
13		19.15	620.49	Siltstone
14		10.67	631.16	Sandy mudstone
15		44.90	676.06	Fine-grained sandstone
16		20.94	697.00	Medium-grained sandstone
17		5.73	702.73	Pebblestone
18		14.68	717.41	Fine-grained sandstone
19		9.11	726.52	Siltstone
20		7.23	733.75	No. 3^{-1} seam
21		15.25	749.00	Sandy mudstone

Figure 2. The histogram of No.18–12 drillhole (Partial) [1].

When the FWF is fully mined and the GSWF reaches its IWS, the roof of the DWFs' gob forms an asymmetrical T-shaped structure (Figure 3). In the FWF area, the IKS I and II fractures give rise to a "double-inclined voussoir beam" along the working face. In contrast, the GSWF exhibits a "single voussoir beam" structure. Only IKS I fractures, while IKS II remains intact, resulting in an overhanging roof. At this time, the intensity of strata behavior of GSWF is relatively low. The roof load shifts to the strata at the working face ends, inducing localized stress concentration and energy accumulation, which provides conditions for inducing the coal bursts in the GSR.

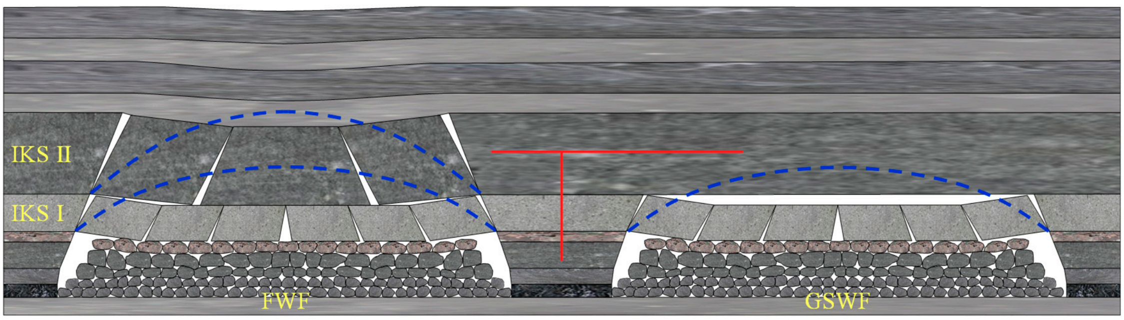

Figure 3. Asymmetrical T-shaped roof structure model of DWFs at the IWS of GSWF.

The GSR preceding the GSWF experiences lateral abutment pressure from the FWF gob that is basically the same across various mining stages. Figure 4 illustrates the distribution pattern of this load.

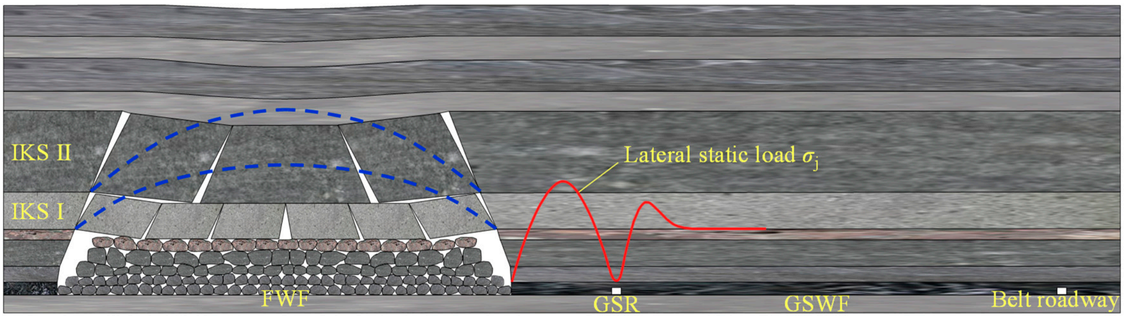

Figure 4. Schematic diagram of the gob side static load distribution in front of GSWF.

According to the literature [1], the lateral static load from the FWF gob on the GSR includes the foundation static load and the mining-induced additional static load:

$$\sigma_j = \sigma_y + \Delta\sigma_I + \Delta\sigma_{II} \tag{1}$$

where σ_j is the lateral static load from the gob on the GSR throughout the FMS of the FWF; σ_y is the foundation static load due to the self-weight of overlying strata; $\Delta\sigma_I$ is the mining-induced additional static load formed by the IKS I; and $\Delta\sigma_{II}$ is the mining-induced additional static load formed by the IKS II.

In Equation (1), σ_y, $\Delta\sigma_I$, and $\Delta\sigma_{II}$ are calculated by Equation (2):

$$\sigma_y = \begin{cases} \frac{\gamma H \tan\alpha}{2(h_0+h_1)+h_2}x & \left(0 \leqslant x \leqslant \frac{2(h_0+h_1)+h_2}{\tan\alpha}\right) \\ \gamma H & \left(x \geqslant \frac{2(h_0+h_1)+h_2}{\tan\alpha}\right) \end{cases} \tag{2}$$

where γ is the strata bulk density; H is the mining depth; α is the strata fracture angle, which can be taken as 70° [37]; and h_0, h_1, and h_2 are the respective thicknesses of the immediate roof, IKS I, and IKS II.

$$\Delta\sigma_I = \begin{cases} \frac{2\sigma_{Imax}\tan\alpha}{2h_0+h_1}x & \left(0 \leqslant x \leqslant \frac{2h_0+h_1}{2\tan\alpha}\right) \\ 2\sigma_{Imax}\left(1 - \frac{\tan\alpha}{2h_0+h_1}x\right) & \left(\frac{2h_0+h_1}{2\tan\alpha} \leqslant x \leqslant \frac{2h_0+h_1}{\tan\alpha}\right) \\ 0 & \left(x \geqslant \frac{2h_0+h_1}{\tan\alpha}\right) \end{cases} \tag{3}$$

where σ_{Imax} is the maximum mining-induced additional static load caused by IKS I.

$$\Delta\sigma_{II} = \begin{cases} \frac{2\sigma_{IImax}\tan\alpha}{2(h_0+h_1)+h_2}x & \left(0 \leqslant x \leqslant \frac{2(h_0+h_1)+h_2}{2\tan\alpha}\right) \\ 2\sigma_{IImax}\left(1 - \frac{\tan\alpha}{2(h_0+h_1)+h_2}x\right) & \left(\frac{2(h_0+h_1)+h_2}{2\tan\alpha} \leqslant x \leqslant \frac{2(h_0+h_1)+h_2}{\tan\alpha}\right) \\ 0 & \left(x \geqslant \frac{2(h_0+h_1)+h_2}{\tan\alpha}\right) \end{cases} \tag{4}$$

where σ_{IImax} is the maximum mining-induced additional static load caused by IKS II.

The formula for calculating σ_{Imax} in Equation (3) is as follows:

$$\sigma_{Imax} = \frac{\frac{1}{2}Q_{zI}}{\frac{2h_0+h_1}{2\tan\alpha}} = \frac{\gamma_1 h_1 l_1 \tan\alpha}{2h_0+h_1} \tag{5}$$

where Q_{zI} is the weight of the fragmented rock mass of IKS I; γ_1 is the bulk density of IKS I; and l_1 is the IKS I breaking interval.

The formula for calculating σ_{IImax} in Equation (4) is as follows:

$$\sigma_{IImax} = \frac{\frac{1}{2}Q_{zII}}{\frac{2(h_0+h_1)+h_2}{2\tan\alpha}} = \frac{(\gamma_2 h_2 + \gamma_3 h_3 K_z) l_2 \tan\alpha}{2(h_0+h_1)+h_2} \tag{6}$$

where Q_{zII} is the weight of the fragmented rock mass of IKS II and the load transferred from the overburden; γ_2 and γ_3 are the bulk density of IKS II and the overlying load layer; h_3 is the thickness of overlying load layer; K_z is the transfer coefficient of overlying load; and l_2 is the IKS II breaking interval.

The lateral static load from the FWF gob on the GSR σ_j can be calculated by Equations (1)–(6).

The GSR surrounding rock in front of the GSWF experiences combined load conditions. These include FWF gob-induced lateral abutment pressure, advanced abutment pressure of the working face, and disturbance dynamic loading caused by breaking thick and hard roofs. When the combined load exceeds the critical threshold for coal and rock bursting failure, coal bursts may occur. The loads at the front of the working face vary during the different stages, necessitating stage-specific analysis of the roof structure to accurately describe the loaded state of the GSR.

Figure 5 illustrates a three-dimensional model of the DWFs' roof during the IWS of the GSWF. It also shows the patterns of different load distributions: the lateral static load σ_j of FWF gob, the advanced static load σ_{jc} of GSWF, and the dynamic load σ_{dc} caused by the fracturing of thick and hard roofs.

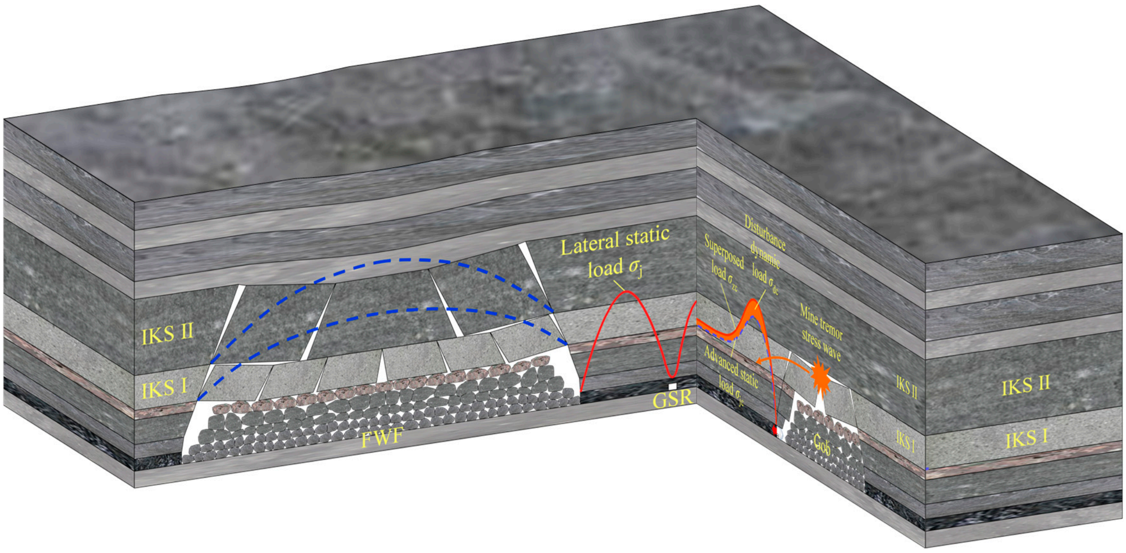

Figure 5. 3D model of the DWFs' roof and "three-load" superposition combined on the GSR at the IWS of the GSWF.

Figure 6 illustrates the roof structure and the combined loading profile in front of the GSWF, extending from the setup entry along the mining direction.

Two main sources of static load on the GSR surrounding rock are present at the IWS of the GSWF. The first source is the lateral static load σ_j, which is induced by the FWF gob. The second source is the advanced static load σ_{jc}, originating from the advanced abutment pressure of the GSWF.

The magnitude and distribution of the abutment pressure of the working face are influenced by various factors such as mining depth, mining height, roof lithology, and its structural characteristics. The distribution of abutment pressure, calculated using the limit equilibrium theory [38–40] in limit equilibrium and elastic zones, is as follows:

$$\sigma_a = \begin{cases} \delta(p + c\cot\varphi)e^{\frac{2\delta f}{m}x} - c\cot\varphi & (0 \leqslant x \leqslant x_0\ ) \\ K'\gamma H e^{\frac{2f}{m\lambda}(x_0 - x)} & (x \geqslant x_0) \end{cases} \tag{7}$$

where $\delta = \frac{1+\sin\varphi}{1-\sin\varphi}$, $x_0 = \frac{m}{2\delta f}\ln\frac{K'\gamma H + c\cot\varphi}{\delta(p + c\cot\varphi)}$; σ_a is the vertical stress; p is the support resistance; δ is the triaxial stress coefficient; and c and φ are the cohesion and friction angle.

Additionally, f is the friction coefficient; m is the mining height; x is the distance to coal rib; x_0 is the limit equilibrium zone width; K' is the stress concentration coefficient; γ is the strata bulk density; and λ is the lateral pressure coefficient.

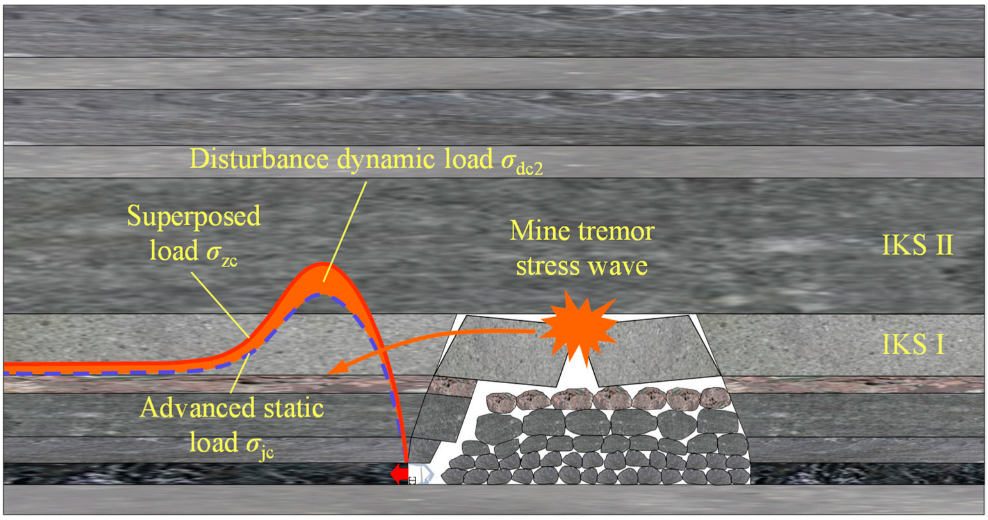

Figure 6. Schematic diagram of dynamic and static loads combined in front of working face at the IWS.

Equation (7) can be used to calculate the advanced static load σ_{jc}, σ_{jz} during the IWS and the PWS (FMS) of the GSWF.

The main source of dynamic load on the GSR surrounding rock at the IWS of the GSWF is the disturbance dynamic load that stems from the IKS I initial failure. Using a calculation approach for the disturbance dynamic load generated by the IKS I failure during the IWS, as per reference [41], the resulting disturbance dynamic load of the GSWF is

$$\sigma_{dc} = 0.0645\rho V_s \left(\eta \frac{{q_c}^2 {l_c}^5}{576EJ}\right)^{0.3566} L^{-\beta} \tag{8}$$

where ρ is the medium density; σ_{dc} is the disturbance dynamic load caused by the IKS I fractures; V_s is the wave velocity; η is the energy conversion coefficient, which can be taken as 0.1% to 1% [42]; q_c is the overlying strata load of IKS I; l_c is the IKS I initial breaking interval; J is the moment of inertia; E is the roof strata elastic modulus; L is the propagation distance; and β is the attenuation index, which can be taken as 1.526 [43].

Based on the above analysis, the total stress on the GSR surrounding rock during the IWS of the GSWF is

$$\sigma_{zc} = \sigma_j + \sigma_{jc} + \sigma_{dc} \tag{9}$$

3.2. Roof Structure and Stress Calculation of Roadway Surrounding Rock During the FMS

The GSWF undergoes several stages as the working face progresses: the IWS, PWS, and FMS. During the PWS, the IKS II fractures and forms a "double-inclined voussoir beam" structure along the working face. This fracture creates a symmetrical T-shaped structure in the roof of the DWFs' gob (Figure 7). The IKS II failure generates dynamic loads on IKS I and the working face. These dynamic loads elevate the potential of coal bursts in the GSR, particularly in areas where the coal and rock mass already experience high-stress concentrations or significant elastic energy accumulation.

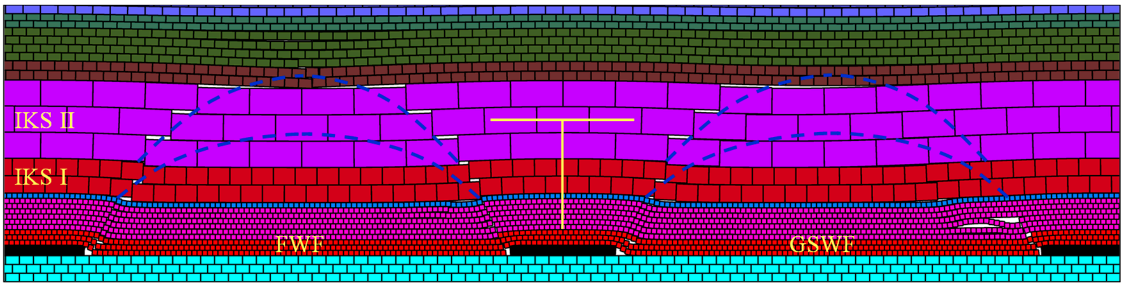

(**a**)

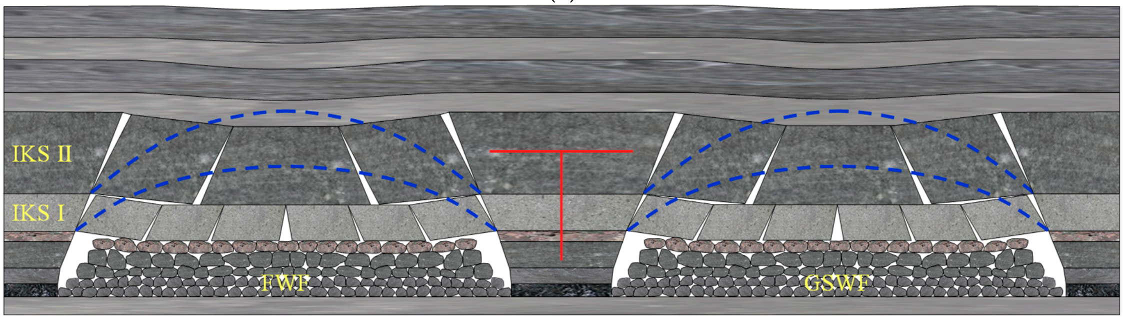

(**b**)

Figure 7. Symmetrical T-shaped roof structure model of the DWFs during the PWS of the GSWF. (**a**) UDEC numerical simulation results of the roof structure form of the DWFs; (**b**) symmetrical T-shaped roof structure model of the DWFs.

Throughout the FMS of the GSWF, the roof of the DWFs' gob forms a symmetrical T-shaped structure, as depicted in Figure 8. Meanwhile, this triggers large-scale movement in the overlying high-position thick and hard strata, leading to energy release within the roof, thereby intensifying the dynamic disturbance exerted by the IKS II on the underlying strata. This intensified disturbance could induce coal bursts in the GSR when the total stress or energy exceeds the critical threshold for burst failure of the coal and rock mass. Therefore, the FMS presents a higher propensity for coal bursts in the GSR compared to the PWS. This increased risk stems from the more intense dynamic loading effect due to the large-scale movement of the overlying strata at the DWFs.

Figure 9 illustrates a three-dimensional model of the DWFs' roof during the IWS of the GSWF. It also shows the patterns of different load distributions: the lateral static load σ_j of the FWF gob, the advanced static load σ_{jz} of the GSWF, and the dynamic load σ_{dz} caused by the fracturing of thick and hard roofs.

Analysis reveals a higher likelihood of coal bursts in the GSR throughout the FMS compared to the PWS. Consequently, we focus on the load status of the GSR in front of the working face at the FMS of the GSWF. Figure 10 exhibits the roof structure and the dynamic and static loads combined along the mining direction as the GSWF reaches the FMS.

At this stage, the static load on the GSR surrounding rock remains comparable to that in the IWS. However, the primary dynamic load source stems from the fracture-induced dynamic load of IKS I and II (Figure 10). Research indicates that the maximum disturbance dynamic load occurs when these two sets of inferior key strata break simultaneously [16]. The stress estimation should take into account the most adverse stress conditions for the surrounding rock, which is determined by the strong disturbance dynamic load generated during the simultaneous fracture of two sets of inferior key strata.

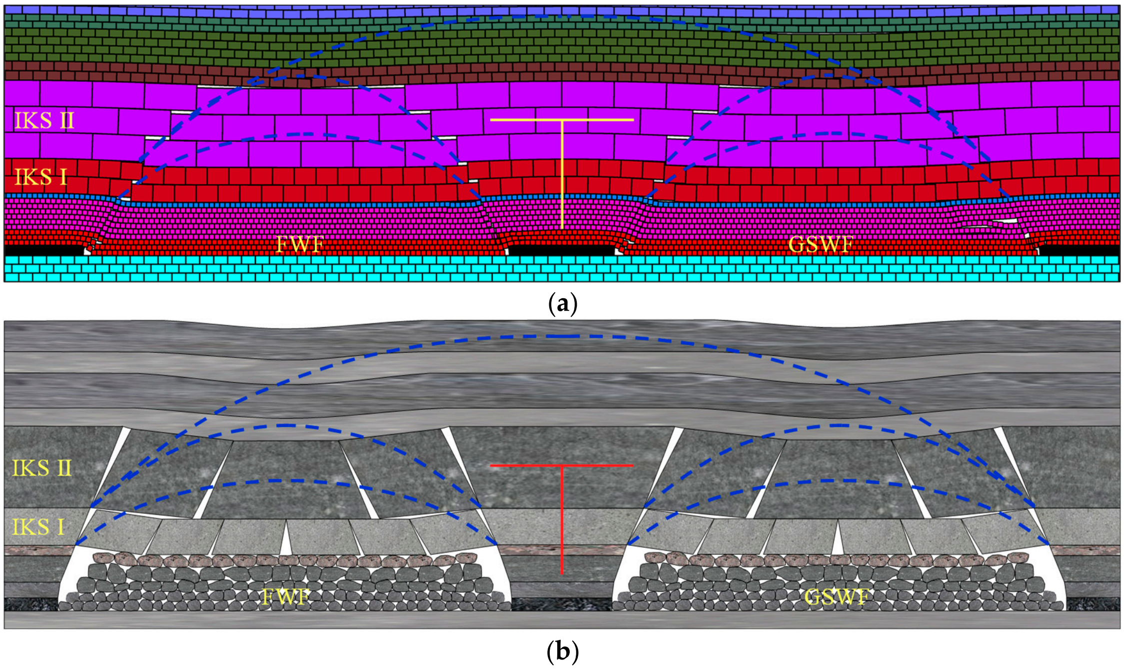

Figure 8. Symmetrical T-shaped roof structure model of the DWFs during the FMS of the GSWF. (**a**) UDEC numerical simulation results of roof structure form of the DWFs; (**b**) symmetrical T-shaped roof structure model of the DWFs.

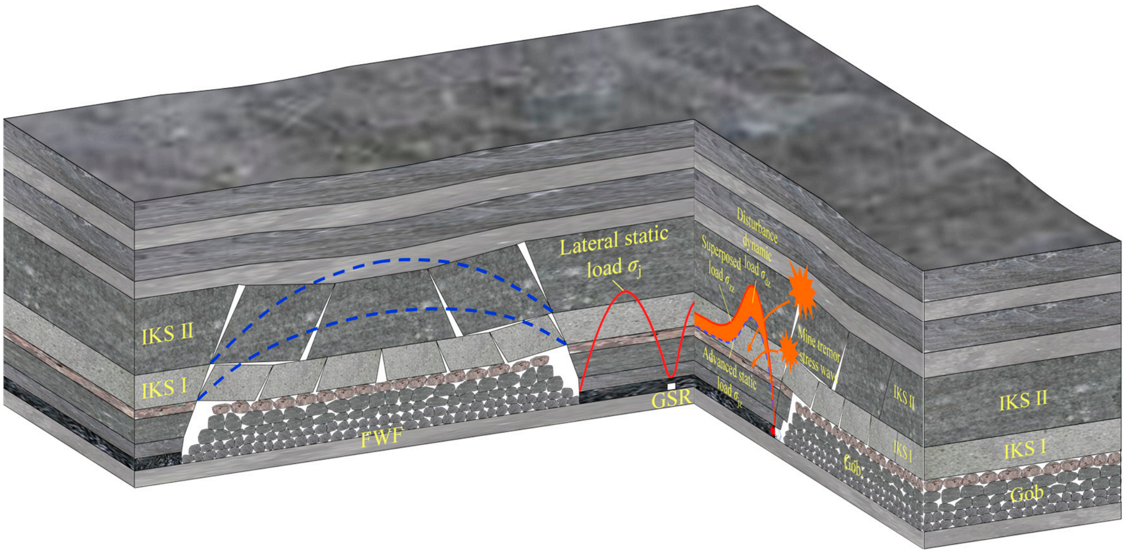

Figure 9. 3D model of the DWFs' roof and "three-load" superposition combined on the GSR at the FMS of the GSWF.

According to the literature [41], the approach of determining the disturbance dynamic load generated by the synchronous fracture of IKS I and II is presented as follows:

$$\begin{aligned}\sigma_{dz} &= 0.0645\rho V_s[\eta(U_{wzI} + U_{wzII})]^{0.3566}L^{-\beta} \\ &= 0.0645\rho V_s\left[\eta\frac{\left(q_{zI}{}^2 l_{zI}{}^5 + q_{zII}{}^2 l_{zII}{}^5\right)}{8EJ}\right]^{0.3566}L^{-\beta}\end{aligned} \quad (10)$$

where q_{zI} and q_{zII} are the overlying strata load of IKS I and II; and l_{zI} and l_{zII} are the periodic breaking intervals of IKS I and II.

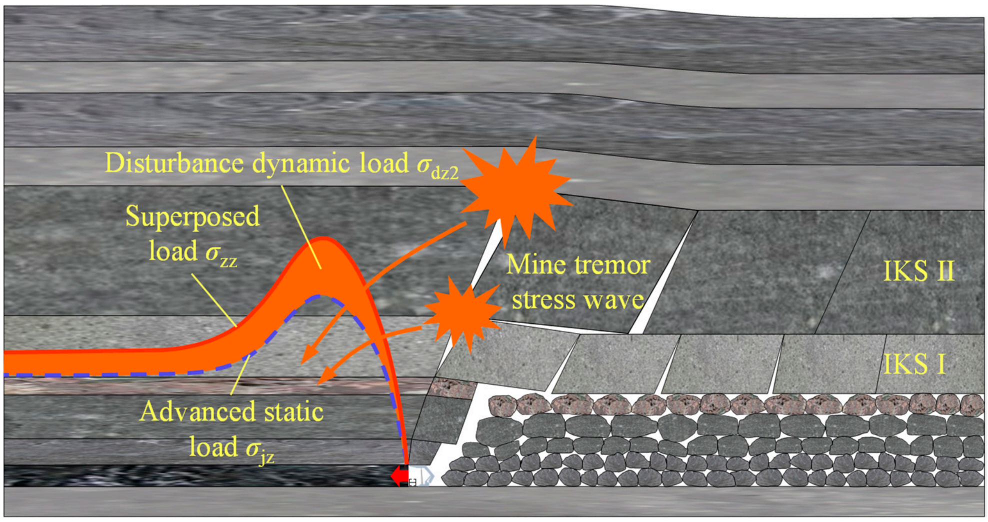

Figure 10. Schematic diagram of dynamic and static loads combined in front of the working face during the FMS.

Based on the above analysis, the total stress on the GSR surrounding rock during the FMS of the GSWF is

$$\sigma_{zz} = \sigma_j + \sigma_{jz} + \sigma_{dz} \tag{11}$$

3.3. Stability Analysis of Roadway Surrounding Rock

The critical stress required for burst failure in a coal and rock mass depends on the coal seam storage conditions and mining methods. Key factors influencing this stress include mining depth, coal and rock lithology, bursting liability, mining district layout, and mining techniques. Assuming that the critical stress for coal and rock burst failure under certain mining conditions as σ_{bmin} [44], the total stress on the GSR surrounding rock during the IWS and FMS of the GSWF, represented as σ_{zc} and σ_{zz}, can be calculated by Equations (9) and (11). Meanwhile, we define an index of burst failure of the GSR surrounding rock K_b, which is the ratio of the difference between the total stress on the GSR surrounding rock σ_{zc} (σ_{zz}) and the support stress of the roadway ψ to the critical stress for coal and rock burst failure σ_{bmin}. The stability of the GSR surrounding rock can be categorized into three cases, as expressed in Equation (12):

(1) Failure: When K_b is greater than 1;
(2) Critical state: When K_b equals 1;
(3) Safe: When K_b is less than 1.

$$K_b = \begin{cases} \frac{\sigma_{zc}(\sigma_{zz})-\psi}{\sigma_{bmin}} > 1 & \text{Failure} \\ \frac{\sigma_{zc}(\sigma_{zz})-\psi}{\sigma_{bmin}} = 1 & \text{Critial State} \\ \frac{\sigma_{zc}(\sigma_{zz})-\psi}{\sigma_{bmin}} < 1 & \text{Safe} \end{cases} \tag{12}$$

4. The Dynamic Changes of Stress and Energy Distributions Induced by Mining Activities

Section 3 analyzes the roof structure throughout the IWS and FMS of the GSWF. It identifies the load sources and characteristics affecting the GSR surrounding rock across different mining stages. A method for calculating the stress on the GSR was proposed, and load characteristics within the GSR surrounding rock during the mining process of the GSWF were quantitatively characterized. To further investigate the stress and energy evolution of the working face and GSR surrounding rock, FLAC^{3D} 5.01 software is employed to investigate the dynamic changes of stress and energy fields in the specified working face and GSR surrounding rock throughout the FMS of the GSWF, considering varying coal pillar widths.

4.1. Numerical Computational Approach

(1) Numerical modeling

A 3D numerical FLAC^{3D} model was constructed using the geological data from the coal mine. This model spans 750 m lengthwise, 800 m across, and 164 m in height, incorporating 1,464,960 grid cells and 1,545,495 nodes, as illustrated in Figure 11. To minimize boundary effects, a 100 m boundary coal pillar was implemented around the model. Due to the significant burial depth of the coal seam, the model may not simulate all overlying strata. To compensate, a vertical stress of 14.8 MPa was applied to the top of the model, calculated based on the depth of the coal seam and the model height. The model employs a fixed bottom boundary and utilizes roll-support boundaries for the remaining surfaces. Based on the in situ stress test results and the literature [45], the coefficient of lateral stress was set to 1.2. The model primarily simulates the stress and energy distribution characteristics of the surrounding rock after working face mining. According to relevant studies [46–48], the Mohr–Coulomb yield criterion was used to determine the failure behavior of the coal and rock mass in the model. Furthermore, the model includes the FWF and the GSWF. Material properties of geological strata employed for the numerical model were sourced from the literature [1] and are listed in Table 1.

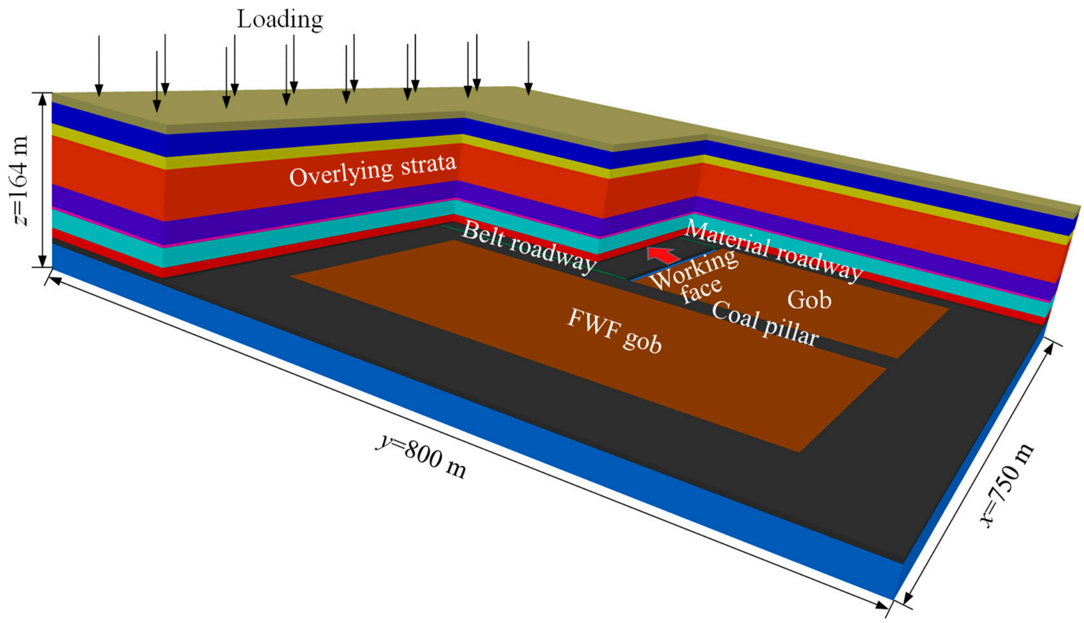

Figure 11. Illustrative representation of the 3D model and DWFs.

(2) Simulation scheme

The simulation process began with excavating the setup entry and roadway within the model. Subsequently, the FWF was excavated to the FMS. Next, the GSWF was excavated step by step at a distance of 10 m, concurrent with backfilling operations. Backfilling of the gob occurred at 10 m following the working face, with each backfill section measuring 210 m long, 10 m wide, and 6.4 m high. Material properties for the backfilling material can be found in Table 1.

Monitoring lines were established at 5, 10, 15, 20, 30, 50, 150, 200, and 250 m in front of the GSWF and the central region within the coal pillar. Concurrently, the monitoring surface was installed on the immediate roof above the working face. These monitoring systems were designed to measure the stress redistribution and energy accumulation in the surrounding rock during the mining process of the working face. By extracting stress values from the monitoring lines and surfaces, theoretical calculations enabled the quantitative characterization of the stress concentration and energy accumulation in the monitored areas. This study investigated the evolution laws of stress and energy at different advance distances of the GSWF with coal pillar widths of 5, 8, 10, 20, 30, and 40 m. A visual representation of the stress monitoring lines around the GSWF is provided in Figure 12.

Table 1. Material properties of the geological strata employed for the numerical model.

Lithology	Density/(kg/m^3)	Shear Modulus/GPa	Bulk Modulus/GPa	Cohesion/MPa	Friction/(°)	Tensile Strength/MPa
Sandy mudstone	2510	4.2	5.6	4.7	34	4.3
Siltstone	2750	5.0	6.9	3.0	32	3.6
Sandy mudstone	2510	3.5	5.2	5.0	33	4.5
Fine-grained sandstone	2650	2.9	3.9	2.8	36	3.5
Medium-grained sandstone	2850	2.4	4.2	3.0	38	3.7
Pebble stone	2600	2.5	4.2	3.2	32	3.0
Fine-grained sandstone	2640	3.3	4.4	3.1	35	2.9
Siltstone	2750	4.5	6.7	2.9	34	3.3
No. 3-1 seam	1380	1.2	2.3	2.6	25	1.3
Sandy mudstone	2470	3.8	4.8	5.0	34	4.6
Backfill material	1700	0.2	1.0	0.4	15	0

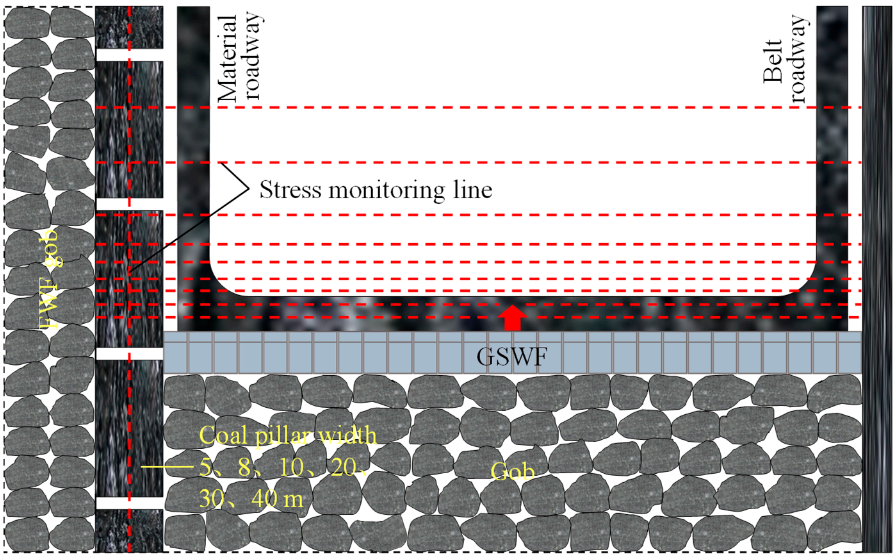

Figure 12. Illustrative representation of stress monitoring lines at GSWF.

4.2. Vertical Stress Variation of Coal Pillars and the GSWF Roof

(1) Influence of secondary mining on the vertical stress distribution within the coal pillar

We analyzed the vertical stress within the coal pillar at various advance distances, considering four typical coal pillar widths of 5, 10, 20, and 40 m. The stress distribution within the coal pillar during the mining process of the GSWF for various coal pillar widths is shown in Figure 13.

Figure 13 illustrates that the excavation of the GSWF has a profound influence on the vertical stress patterns within coal pillars. This impact varies depending on the coal pillar width. Notably, the stress experienced by the coal pillar during the secondary mining stage exceeds that of the first mining stage. After the excavation of the first working face, vertical stress concentrates in the coal pillar area, potentially causing plastic deformation. Subsequent excavation of the adjacent working face results in superposition of secondary mining-induced stress in the coal pillar area. Consequently, the vertical stress within the coal pillars increases. Furthermore, the adjacent DWFs form a symmetrical T-shaped structure in the gob area, leading to the complete fracturing of the overlaying strata. Consequently, these fractured layers impose a substantial load on the coal pillar. This leads to a marked increase in the vertical stress within the coal pillar. Meanwhile, the vertical stress in the coal pillar also rises within about 150 m in front of the working face. Consequently, high stress concentrates on the coal pillar side of the GSR. This stress concentration often leads to dynamic pressure behavior in the GSR and, in extreme cases, may trigger coal bursts. With a coal pillar width of 5 m, vertical stresses ranged from 7.42 to 9.45 MPa, exhibiting a maximum growth rate of 30.89% compared to the first mining stage. The coal pillar width being increased to 10 m led to higher vertical stresses, reaching 18.97 to 23.23 MPa, though the maximum growth rate decreased to 22.54%. Further widening to 20 m coal pillars caused a significant increase in vertical stress, ranging from 36.96 to 52.15 MPa, with the maximum growth rate rising to 27.92%. Notably, the 40 m coal pillar width showed lower vertical stresses of 31.40 to 42.28 MPa, with the lowest maximum growth rate of 22.33% compared to the first mining stage. Within the simulated range, vertical stress in the coal pillar side on the GSR under secondary mining initially increases with coal pillar width, then decreases. This pattern generates stress relief areas with lower vertical stress. Consequently, placing roadways in stress relief areas can create a low static load condition. Under the same conditions of dynamic load disturbance, the potential risk of coal bursts in the roadway can be reduced.

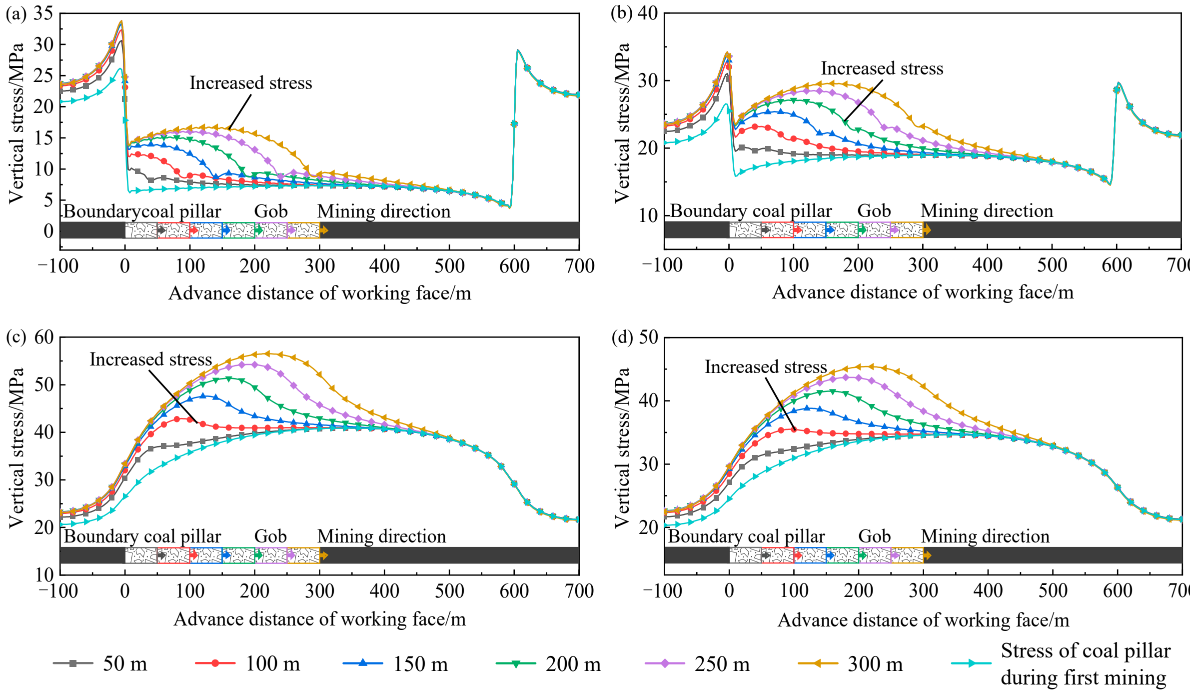

Figure 13. Vertical stress distribution within the coal pillar, influenced by varying coal pillar widths and advance distances under the secondary mining: (**a**) 5 m; (**b**) 10 m; (**c**) 20 m; (**d**) 40 m.

(2) Vertical stress variation of the working face roof

By arranging stress monitoring lines at different positions in front of the working face, we can observe the changes in the vertical stress of the roofs in front of the working face under varying coal pillar widths. Illustrative examples of this are presented in Figure 14, showcasing four typical simulation results with the coal pillar widths of 5, 10, 20, and 40 m.

The visual representation in Figure 14 shows an asymmetric pattern of vertical stress distribution in front of the GSWF with varying coal pillar widths. This asymmetry, characterized by higher stress on the left side, results from the influence of the adjacent FWF gob. This concentrated vertical stress in the roof at the gob-side end of the GSWF induces high static loads on the GSR surrounding rock within approximately 300 m in front of the working face. This concentrated stress significantly contributes to an increased risk of coal bursts in the GSR. With increasing distance from the working face, the vertical stress in the coal pillar and the immediate roof above the working face initially increases before subsequently decreasing. As observed, maximum vertical stress above the working face is located approximately 15 m in front of the working face. Beyond this point, this vertical stress decreases at a rate of about 0.06 MPa/m, as depicted in Figure 15a. With the coal pillar width increasing within this simulated range, the corresponding vertical stress initially rises, followed by a subsequent decline with a corresponding increase in the coal pillar widths. This non-linear relationship suggests that an optimal coal pillar width exists to minimize stress concentrations. The maximum vertical stress in roofs at the gob-side end in the GSWF spans from 40.18 to 49.80 MPa and exhibits a negative linear correlation with coal pillar width. The relationship follows the equation C), where B is the coal pillar width. This suggests a stress diminution rate of roughly 0.30 MPa/m expansion in coal pillar width. In a similar vein, the concentration coefficient of vertical stress on the roof fluctuates between 2.20 and 2.73, demonstrating a linear decline as the coal pillar width expands. This relationship is described by $K_S = -0.02B + 2.84$ ($R^2 = 0.98$), signifying a decrease of 0.02 units in K_S for every meter of expansion in the coal pillar width (Figure 15b).

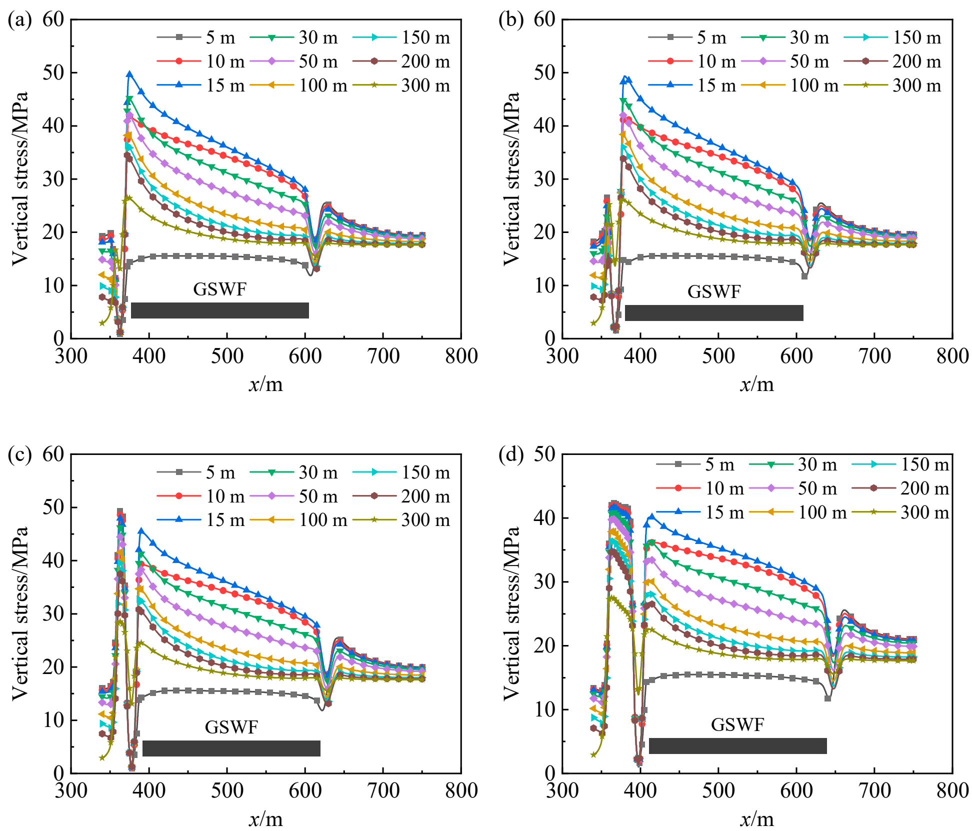

Figure 14. Changes in vertical stress in front of the working face influenced by varying coal pillar widths: (**a**) 5 m; (**b**) 10 m; (**c**) 20 m; (**d**) 40 m.

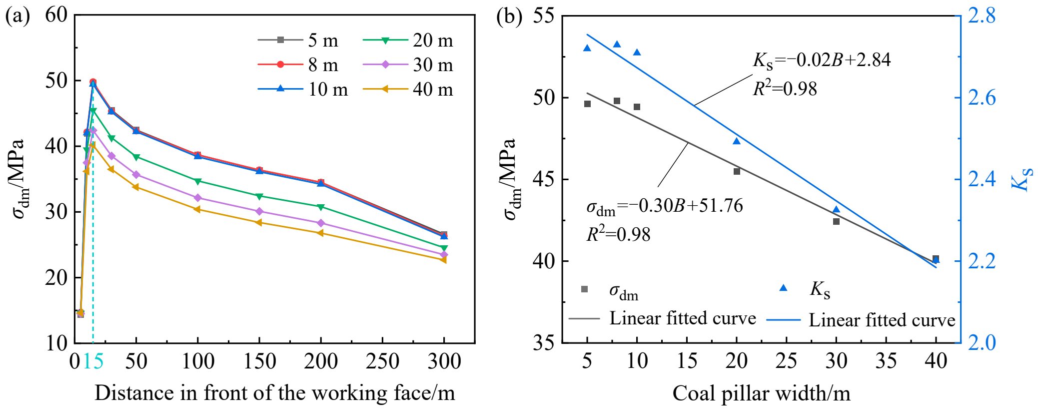

Figure 15. Changes in peak values and concentration coefficient of vertical stress on the roof, influenced by varying coal pillar widths: (**a**) Changes in peak values of vertical stress observed at various points in front of working face; (**b**) Changes in peak values and concentration coefficient of vertical stress.

4.3. Energy Density Distribution of GSWF Roof

A primary factor triggering coal bursts is the abrupt discharge of the substantial energy stored within the surrounding rock of the stope [13,22,33,49–51]. Multiple factors influence the energy distribution in the surrounding rock of the stope. While the characteristics and magnitude of ground stress are important factors [52,53] affecting the energy levels in the surrounding rock of the stope, horizontal stress does not significantly impact the overall energy distribution pattern under specific ground stress conditions. By strategically positioning stress monitoring surfaces within the roof to acquire the three principal stress data of the roof layers in the stope with varying coal pillar widths, the energy density value of the roof strata can be computed using Equation (13) [49,54–57].

$$u = \frac{1}{2E}\left[\sigma_1^2 + \sigma_2^2 + \sigma_3^2 - 2\mu(\sigma_1\sigma_2 + \sigma_2\sigma_3 + \sigma_3\sigma_1)\right] \quad (13)$$

where u is the energy density; E is the elastic modulus; and μ is Poisson's ratio.

The energy density of different areas in the roof under four typical coal pillar widths of 5, 10, 20, and 40 m is analyzed, and the distribution pattern is illustrated in Figure 16.

Figure 16 illustrates the varying degrees of energy accumulation in the roof of the gob-side end of the GSWF (the blue "triangle" area) for varying coal pillar widths. If the coal pillar width exceeds 20 m, energy accumulation also occurs within the coal pillar behind the working face. This energy accumulation pattern exhibits a notable trend: with the coal pillar width increasing, the amount of energy accumulated within the coal pillar behind the working face gradually decreases. The relationship between the peak values of energy density at the gob-side end of the working face and coal pillar widths demonstrates a linear negative correlation. Within the simulated coal pillar widths range, the peak values of energy density vary from 52.54 to 74.81 MJ/m^3. This relationship is described by $E_m = -0.67B + 78.66$ ($R^2 = 0.97$), where E_m is the maximum energy density and B is the coal pillar width. The peak energy density decreases at a rate of 0.67 (MJ/m^3)/m corresponding to an increasing coal pillar width (Figure 17). The coefficient of energy accumulation, defined as the ratio of the peak values of energy density in the roof after coal mining to the initial energy density in the roof before coal mining, also exhibits an inverse relationship with coal pillar width. This coefficient ranges from 3.20 to 4.56 and follows $K_e = -0.04B + 4.80$ ($R^2 = 0.96$), where K_e is the coefficient of energy accumulation. The coefficient of energy accumulation decreases at a rate of 0.04/m increase with the coal pillar width (Figure 17).

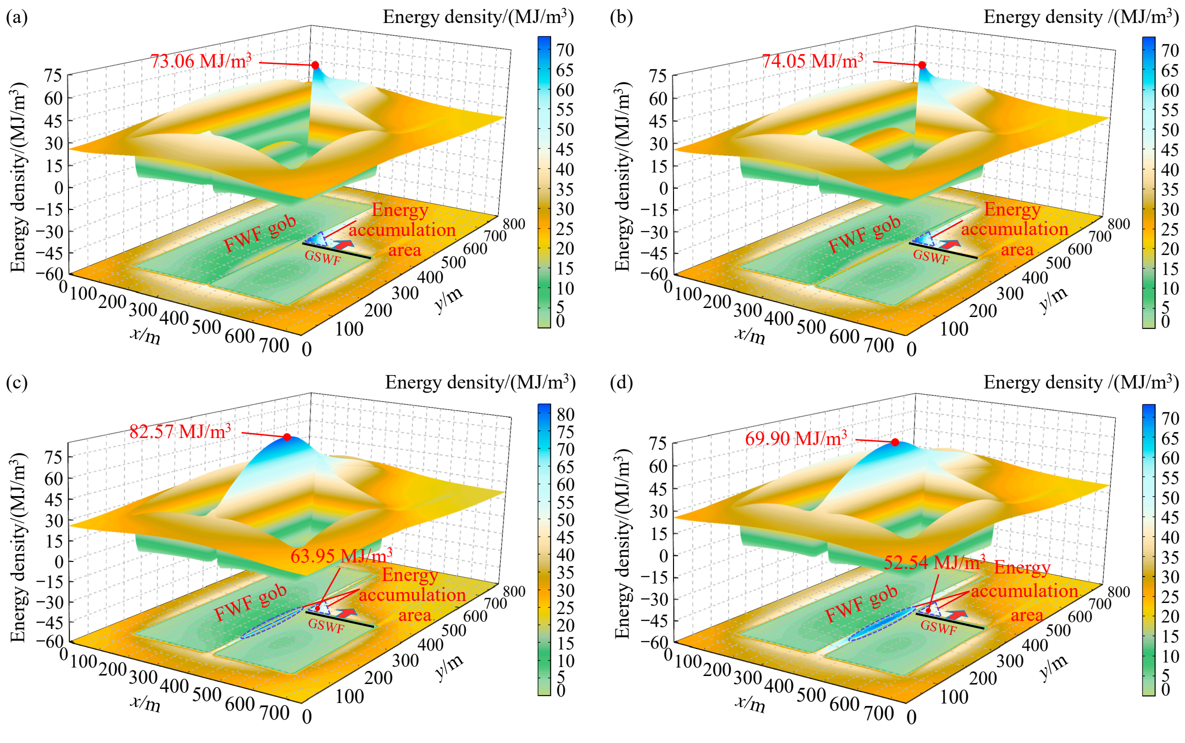

Figure 16. The energy density distribution at the working face roof under various coal pillar widths: (**a**) 5 m; (**b**) 10 m; (**c**) 20 m; (**d**) 40 m.

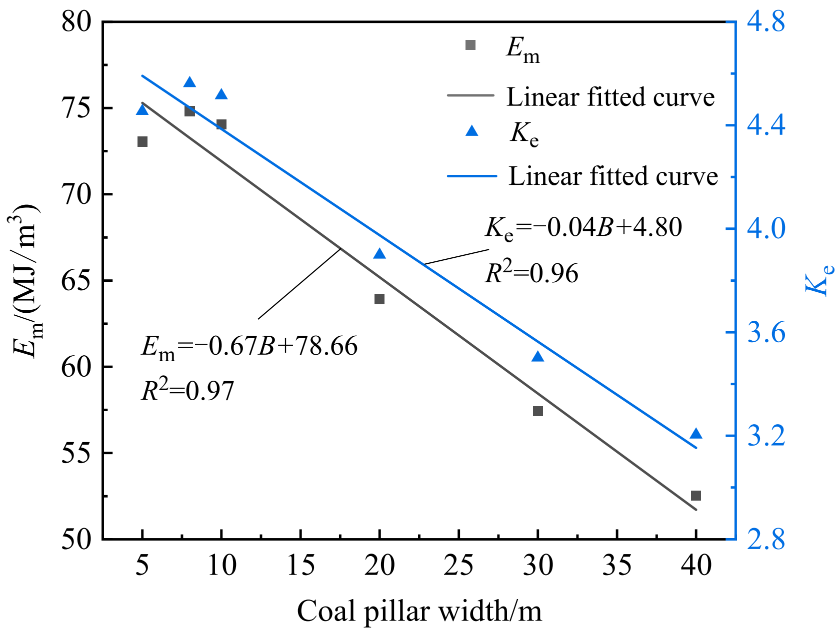

Figure 17. Changes in peak values of energy density and coefficient of energy accumulation across various coal pillar widths.

Changes in the peak values of both vertical stress and energy density within the roof, as well as the vertical stress within the coal pillar at the gob-side end of the GSWF, considering the coal pillar widths of 5, 8, 10, 20, 30, and 40 m, are illustrated in Figure 18.

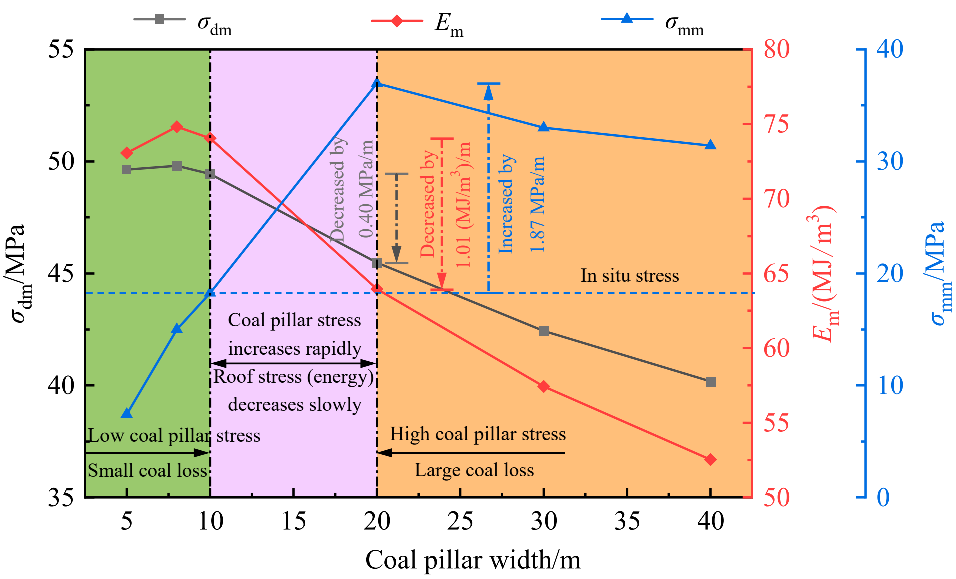

Figure 18. Changes in maximum vertical stress and energy density within the immediate roof, along with vertical stress in coal pillar, across varying coal pillar widths.

As illustrated in Figure 18, when the coal pillar width is less than 20 m, reducing the coal pillar width can reduce the overall pressure in the coal pillar and improve stress conditions within the GSR. However, both the vertical stress as well as the energy density in the immediate roof at the gob-side end above the working face will increase, affecting the overall loading status of the GSR. Therefore, the above factors should be considered when selecting the optimal coal pillar width to reduce the static load on the GSR surrounding rock and reduce potential burst failure within the roadway. For coal pillar widths of 5–10 m, the vertical stress in coal pillar remains below in situ stress levels, creating a reduced stress area. Such a condition facilitates effective management of the GSR surrounding rock while minimizing resource loss in the designated coal pillar. Within the range of coal pillar widths from 10–20 m, an increase in coal pillar width corresponds to a rise in the vertical stress in the coal pillar of approximately 1.87 MPa/m. Concurrently, the maximum vertical stress and energy density within the roof at the gob-side extremity of the working face decrease at rates of 0.40 MPa/m and 1.01 $(MJ/m^3)/m$, respectively. The rise in vertical stress attributed to the coal pillar width is more significant, and the overall stress conditions within the GSR become poor. For coal pillar widths ranging from 20–40 m, maximum levels of both vertical stress and energy density within the immediate roof, as well as peak values of vertical stress within the coal pillar, all decrease at varying rates with the coal pillar width increases. However, the peak vertical stress experienced by the coal pillar remains above the in situ stress levels, approximately 1.72 to 2.03 times these in situ stress levels. This is accompanied by significant resource loss within the reserved coal pillar. Considering the vertical stress within the coal pillar, vertical stress and energy density within the roof at the gob-side extremity of the working face, and resource loss caused by the reserved coal pillar, we can conclude that a reasonable coal pillar width is 5 to 10 m. At the same time, the roof support at the gob-side end of the working face should be strengthened in order to improve the overall stability of the GSR, thereby reducing the chance of coal bursts in the GSR.

5. Discussions

Section 3 analyzed the morphology of roof structures during the IWS and FMS of the GSWF. It explored how these varying roof structures apply loads to the GSR surrounding rock. Despite the different mining stages, the static loads of the advanced working face area in the GSR remain relatively consistent. These loads primarily consist of the lateral static load from the gob and advanced static load of the working face. The lateral static load from the gob increases initially and then decreases with distance from the gob. Consequently, advanced static load on the solid coal side of the GSR shows an asymmetric stress distribution [58]. Stresses are highest near the gob and decrease further away; this evolution law is consistent with the numerical simulation results of vertical stress distribution in front of the working face shown in Figure 14. Furthermore, the theoretical analysis of stress distribution based on the roof structure aligns with the numerical simulation results.

The load transmitted from the roof fracture of the adjacent gob to the advanced area of the solid coal side of the GSR is related to the coal pillar width and the distance to the GSWF. When the coal pillar width is small, the lateral roof of the adjacent gob transmits a large load to the solid coal side of the GSR. Additionally, when the distance to the GSWF is small, the load on the solid coal side of the GSR in front of the working face transmitted from the GSWF is relatively large [29,47,59]. These loads accumulate, leading to energy accumulation in this region (Figures 5 and 9). The accumulated energy decreases as the coal pillar width and the distance to the GSWF increase. This trend aligns with the numerical simulation results, which show the energy density distribution of the roof in front of the working face (Figure 16). The theoretical analyses are consistent with numerical simulation results, confirming the reliability of both approaches.

The analysis of the roof structures of the GSWF and its loading characteristics on the surrounding rock of the GSWF and GSR, as discussed in Section 3, is grounded in classic mine pressure theory and key strata theory [10]. While variations in stratigraphic configurations, lithology, and mining conditions lead to differences in the roof structures, they also make a difference in the load characteristics and stress-energy levels in the GSR. Despite these differences, the results presented in this paper are broadly applicable and reflect typical patterns. They offer valuable insights for studying and preventing coal bursts in GSRs under similar geological and mining conditions.

6. Conclusions

This study establishes a model of the roof structure during various mining stages within the GSWF, analyzes various load sources of the GSR, proposes a method for calculating stress within the GSR surrounding rock, and further discusses how the roof configuration form influences the stability of the GSR. Numerical simulations analyze dynamic changes in the mining-induced stress and energy fields within the working face, coal pillar, and GSR surrounding rock during the mining process of the GSWF. Key findings from this study include the following:

(1) Throughout the IWS in the GSWF, the roof of the DWFs forms an asymmetrical T-shaped structure along the working face orientation. During this stage, the intensity of the strata behavior of the GSWF is relatively low and the roof load is transferred to strata at the working face on both ends. Stress concentration, accompanied by energy accumulation, occurs in local areas, posing a risk of coal bursts in the GSR. Throughout the FMS of the GSWF, the roof of the DWFs forms a symmetrical T-shaped structure along the working face orientation. The breaking of IKS II causes dynamic loads on IKS I, the working face itself, and the working face on both ends, which can easily induce coal bursts in the GSR.

(2) A combined dynamic and static loading mechanical model for the GSR in front of the working face throughout both the IWS and FMS was developed. Additionally, a "three-load" dynamic and static load superposition principle applicable to the GSR was proposed, based on the lateral static load of the adjacent gob, the advanced static load originating from the working face, and the associated dynamic load. A calculation method for stress distribution within the GSR surrounding rock during various mining stages in the GSWF was obtained, and load characteristics within the GSR surrounding rock throughout the mining process of the GSWF were quantitatively characterized. The index of burst failure of GSR surrounding rock was proposed, and the criterion for judging the burst failure of roadways was established.

(3) Numerical calculation reveals that the vertical stress within the coal pillar in front of the GSWF increases compared to the first mining stage, causing a high stress concentration on the coal pillar side in the specified GSR in front of the working face. The elevated stress levels contribute to energy accumulation in the roof at the gob-side end of the GSWF, potentially leading to dynamic pressure in the roadway and, in extreme cases, coal bursts. As the distance to the working face increases, both the vertical stress within the coal pillar and the roof first rise, then decline. Furthermore, the vertical stress within the coal pillar initially rises and subsequently declines as coal pillar widths increase. Reducing the coal pillar width appropriately can improve its stress state.

(4) Considering the vertical stress within the coal pillar, the vertical stress and energy density within the roof at the gob-side end of the working face, and resource loss due to the presence of the coal pillar, the ideal coal pillar width should range between 5 and 10 m. Meanwhile, the roof support at the gob-side end of the working face should be strengthened to enhance the overall stability of the GSR surrounding rock, thereby reducing the potential for coal bursts in the GSR.

Author Contributions: J.Z. drafted the manuscript. J.P. and Y.X. provided the technical guidance. W.L., T.D., and J.W. provided writing guidance. All authors have read and agreed to the published version of the manuscript.

Funding: The research is financially supported by the National Key Research and Development Program of China (No. 2022YFC3004604) and the National Natural Science Foundation of China (No. 52174118).

Institutional Review Board Statement: Not Applicable.

Informed Consent Statement: Not Applicable.

Data Availability Statement: The data presented in this study are available on request from the corresponding author. The data are not publicly available due to privacy.

Acknowledgments: The first author would like to thank the Yixin Zhao at China University of Mining and Technology (Beijing), China.

Conflicts of Interest: The authors declare no conflict of interest.

References

1. Zhao, Y.; Zhou, J.; Zhang, C.; Liu, B.; Ling, C.; Liu, W.; Han, C. Failure Mechanism of Gob-Side Roadway in Deep Coal Mining in the Xinjie Mining Area: Theoretical Analysis and Numerical Simulation. *J. Cent. South Univ.* **2023**, *30*, 1631–1648. [CrossRef]
2. Qian, M.; Shi, P.; Xu, J. *Mine Pressure and Ground Control*; China University of Mining and Technology Press: Xuzhou, China, 2010.
3. Ju, J.; Xu, J.; Zhu, W. Longwall Chock Sudden Closure Incident below Coal Pillar of Adjacent Upper Mined Coal Seam under Shallow Cover in the Shendong Coalfield. *Int. J. Rock Mech. Min. Sci.* **2015**, *77*, 192–201. [CrossRef]
4. Ju, J.; Xu, J. Structural Characteristics of Key Strata and Strata Behaviour of a Fully Mechanized Longwall Face with 7.0m Height Chocks. *Int. J. Rock Mech. Min. Sci.* **2013**, *58*, 46–54. [CrossRef]
5. Wang, F.; Xu, J.; Xie, J. Effects of Arch Structure in Unconsolidated Layers on Fracture and Failure of Overlying Strata. *Int. J. Rock Mech. Min. Sci.* **2019**, *114*, 141–152. [CrossRef]
6. Unrug, K.S.B. Methods of Roof Cavability Prediction. *State Art Gr. Control Longwall Min. Min. Subsid.* **1982**, *3*, 13–29.
7. Kratzsch, H. *Mining Subsidence Engineering*; Springer Science & Business Media: Berlin, Germany, 2012.
8. Chien, M. A Study of the Behaviour of Overlying Strata in Longwall Mining and Its Application to Strata Control. *Dev. Geotech. Eng.* **1981**, *32*, 13–17.
9. Qian, M. Conditions Required for Equilibrium of Overlying Strata at Working Areas. *J. China Inst. Min. Technol.* **1981**, *2*, 31–40.
10. Qian, M.; Miao, X.; Xu, J. Theoretical Study of Key Stratum in Ground Control. *J. China Coal Soc.* **1996**, *21*, 225–230.
11. Song, Z. Rules for the Stope Bearing Pressure and Its Application. *J. Shandong Inst. Min. Technol.* **1982**, *1*, 1–25.
12. He, M.; Zhu, G.; Guo, Z. Longwall Mining "Cutting Cantilever Beam Theory" and 110 Mining Method in China-The Third Mining Science Innovation. *J. Rock Mech. Geotech. Eng.* **2015**, *7*, 483–492. [CrossRef]
13. He, M.; Wang, Q. Rock Dynamics in Deep Mining. *Int. J. Min. Sci. Technol.* **2023**, *33*, 1065–1082. [CrossRef]
14. He, M.; Wang, Q.; Wu, Q. Innovation and Future of Mining Rock Mechanics. *J. Rock Mech. Geotech. Eng.* **2021**, *13*, 1–21. [CrossRef]
15. Dou, L.M.; He, X.Q.; He, H.; He, J.; Fan, J. Spatial Structure Evolution of Overlying Strata and Inducing Mechanism of Rockburst in Coal Mine. *Trans. Nonferrous Met. Soc. China* **2014**, *24*, 1255–1261. [CrossRef]

16. Huang, Q.; Zhou, J.; Cao, J. Key Stratum Structure and Support Working Resistance of Longwall Face with Large Mining Height in the Shallow Coal Seams, China. *Adv. Civ. Eng.* **2020**, *2020*, 8834403. [CrossRef]
17. Yu, B.; Zhu, W.; Gao, R.; Liu, J. Strata Structure and Its Effect Mechanism of Large Space Stope for Fullymechanized Sublevel Caving Mining of Extremely Thick Coal Seam. *J. China Coal Soc.* **2016**, *41*, 571–580.
18. Yu, B.; Gao, R.; Kuang, T.; Huo, B.; Meng, X. Engineering Study on Fracturing High-Level Hard Rock Strata by Ground Hydraulic Action. *Tunn. Undergr. Sp. Technol.* **2019**, *86*, 156–164. [CrossRef]
19. Sun, Y.; Zuo, J.; Karakus, M.; Wang, J. Investigation of Movement and Damage of Integral Overburden during Shallow Coal Seam Mining. *Int. J. Rock Mech. Min. Sci.* **2019**, *117*, 63–75. [CrossRef]
20. Zuo, J.; Wang, J.; Jiang, Y. Macro/Meso Failure Behavior of Surrounding Rock in Deep Roadway and Its Control Technology. *Int. J. Coal Sci. Technol.* **2019**, *6*, 301–319. [CrossRef]
21. Zuo, J.; Xu, C.; Sun, Y.; Li, Y.; Wu, G.; Yu, M. Theoretical Model and Verification of "Analogous Hyperbola (Hyperboloid)" for the Overall Movement of Mining Rock Strata: From Two-Dimensional "Analogous Hyperbola" to Three-Dimensional "Analogous Hyperboloid" Models. *J. China Coal Soc.* **2024**, *49*, 1731–1751.
22. Pan, Y.; Song, Y.; Luo, H.; Xiao, Y. Coalbursts in China: Theory, Practice and Management. *J. Rock Mech. Geotech. Eng.* **2024**, *16*, 1–25. [CrossRef]
23. He, M.; Cheng, T.; Qiao, Y.; Li, H. A Review of Rockburst: Experiments, Theories, and Simulations. *J. Rock Mech. Geotech. Eng.* **2023**, *15*, 1312–1353. [CrossRef]
24. Dai, L.; Pan, Y.; Xiao, Y.; Wang, A.; Wang, W.; Wei, C. Parameter Design Method for Destressing Boreholes to Mitigate Roadway Coal Bursts: Theory and Verification. *Rock Mech. Rock Eng.* **2024**, 1–18. [CrossRef]
25. Zhang, J.; Zhang, Y.; Han, Y.; Fan, W.; Song, Z.; Yu, H.; Zhang, J.; Zhang, H.; Liu, J. Study on Stress Distribution Law of Surrounding Rock of Roadway under the Goaf and Mechanism of Pressure Relief and Impact Reduction. *Eng. Fail. Anal.* **2024**, *160*, 108210. [CrossRef]
26. Zhou, K.; Dou, L.; Li, X.; Song, S.; Cao, J. Coal Burst and Mining-Induced Stress Evolution in a Deep Isolated Main Entry Area–A Case Study. *Eng. Fail. Anal.* **2022**, *137*, 106289. [CrossRef]
27. Zhang, Z.; Li, Z.; Xu, G.; Gao, X.; Liu, Q.; Li, Z.; Liu, J. Lateral Abutment Pressure Distribution and Evolution in Wide Pillars under the First Mining Effect. *Int. J. Min. Sci. Technol.* **2023**, *33*, 309–322. [CrossRef]
28. Bai, J.; Shen, W.; Guo, G.; Wang, X.; Yu, Y. Roof Deformation, Failure Characteristics, and Preventive Techniques of Gob-Side Entry Driving Heading Adjacent to the Advancing Working Face. *Rock Mech. Rock Eng.* **2015**, *48*, 2447–2458. [CrossRef]
29. Zhang, G.; Wen, Z.; Liang, S.; Tan, Y.; Tian, L.; Zhao, Y.; Zhao, D. Ground Response of a Gob-Side Entry in a Longwall Panel Extracting 17 m-Thick Coal Seam: A Case Study. *Rock Mech. Rock Eng.* **2020**, *53*, 497–516. [CrossRef]
30. Lou, J.; Gao, F.; Yang, J.; Ren, Y.; Li, J.; Wang, X.; Yang, L. Characteristics of Evolution of Mining-Induced Stress Field in the Longwall Panel: Insights from Physical Modeling. *Int. J. Coal Sci. Technol.* **2021**, *8*, 938–955. [CrossRef]
31. Wang, Z.; Wang, J.; Yang, S. An Ultrasonic-Based Method for Longwall Top-Coal Cavability Assessment. *Int. J. Rock Mech. Min. Sci.* **2018**, *112*, 209–225. [CrossRef]
32. Wang, Z.; Yang, S.; Tang, Y.; Sun, W.; Shui, Y. A Stress Rotation-Based Method for Improving Roof Stability of a Deep Longwall Panel. *Int. J. Geomech.* **2023**, *23*, 04023085. [CrossRef]
33. Ma, Z.; Li, S.; Zhao, X. Energy Accumulation Characteristics and Induced Rockburst Mechanism of Roadway Surrounding Rock under Multiple Mining Disturbances: A Case Study. *Sustainability* **2023**, *15*, 9595. [CrossRef]
34. Zhou, J.; Pan, J.; Xia, Y.; Du, T.; Liu, W.; Zhang, C. Mechanism and Prevention of Coal Bursts in Gob-side Roadway Floor under Thick and Hard Roof in the Deep Mining Area of Ordos. *Int. J. Coal Sci. Technol.* **2024**, *11*, 60.
35. Han, Z.; Dou, L.; Gong, S.; Kan, J.; Chen, S.; He, X. Mechanism of Rock Burst in Deep Gob-Side Entry Based on Dynamic and Static Stress: A Case Study. *Geomat. Nat. Hazards Risk* **2023**, *14*, 2271636. [CrossRef]
36. Bai, J.; Dou, L.; Li, X.; Ma, X.; Lu, F.; Han, Z. Evolution Laws of Stress–Energy and Progressive Damage Mechanisms of Surrounding Rock Induced by Mining Disturbance. *Appl. Sci.* **2023**, *13*, 7759. [CrossRef]
37. Sun, Y.; Zuo, J.; Karakus, M.; Wen, J. A Novel Method for Predicting Movement and Damage of Overburden Caused by Shallow Coal Mining. *Rock Mech. Rock Eng.* **2020**, *53*, 1545–1563. [CrossRef]
38. Zhu, S.; Feng, Y.; Jiang, F. Determination of Abutment Pressure in Coal Mines with Extremely Thick Alluvium Stratum: A Typical Kind of Rockburst Mines in China. *Rock Mech. Rock Eng.* **2016**, *49*, 1943–1952. [CrossRef]
39. Zhang, P.; Sun, B. Distribution Characteristics of the Advance Abutment Pressure in a Deep Stope. *J. Geophys. Eng.* **2020**, *17*, 686–699. [CrossRef]
40. Zhu, Q.; Sui, L.; Yin, Y.; Liu, J.; Ouyang, Z.; Wang, D. Mechanism and Empirical Study of Rockburst in the Adjacent Area of a Fully Mechanized Top-Coal Caving Face Based on Microseismic Technology. *Appl. Sci.* **2023**, *13*, 6317. [CrossRef]
41. Zhao, Y.; Zhou, J.; Liu, W. Characteristics of Ground Pressure and Mechanism of Coal Burst in the Gob Side Roadway at Xinjie Deep Mining Area. *J. China Coal Soc.* **2020**, *45*, 1595–1606.
42. Dou, L.; He, X. *Theory and Technology of Rock Burst Prevention*; China University of Mining and Technology Press: Xuzhou, China, 2001.
43. He, J.; Dou, L.; Cai, W.; Li, Z.; Ding, Y. In Situ Test Study of Characteristics of Coal Mining Dynamic Load. *Shock Vib.* **2015**, *2015*, 121053. [CrossRef]

44. Cai, W.; Bai, X.; Si, G.; Cao, W.; Gong, S.; Dou, L. A Monitoring Investigation into Rock Burst Mechanism Based on the Coupled Theory of Static and Dynamic Stresses. *Rock Mech. Rock Eng.* **2020**, *53*, 5451–5471. [CrossRef]
45. Li, X.; Zhou, Z.; Lok, T.S.; Hong, L.; Yin, T. Innovative Testing Technique of Rock Subjected to Coupled Static and Dynamic Loads. *Int. J. Rock Mech. Min. Sci.* **2008**, *45*, 739–748. [CrossRef]
46. Chang, L.; Konietzky, H. Application of the Mohr-Coulomb Yield Criterion for Rocks with Multiple Joint Sets Using Fast Lagrangian Analysis of Continua 2D (FLAC2D) Software. *Energies* **2018**, *11*, 614. [CrossRef]
47. He, W.; He, F.; Zhao, Y. Field and Simulation Study of the Rational Coal Pillar Width in Extra-Thick Coal Seams. *Energy Sci. Eng.* **2020**, *8*, 627–646. [CrossRef]
48. He, X.; Zhang, C.; Han, P. Overburden Damage Degree-Based Optimization of High-Intensity Mining Parameters and Engineering Practices in China's Western Mining Area. *Geofluids* **2020**, *2020*, 8889663. [CrossRef]
49. Du, F.; Ma, J.; Guo, X.; Wang, T.; Dong, X.; Li, J.; He, S.; Nuerjuma, D. Rockburst Mechanism and the Law of Energy Accumulation and Release in Mining Roadway: A Case Study. *Int. J. Coal Sci. Technol.* **2022**, *9*, 67. [CrossRef]
50. Das, A.J.; Mandal, P.K.; Ghosh, N.; Singh, A.P.; Kumar, R.; Tewari, S.; Bhattacharjee, R. Evaluation of Energy Accumulation, Strain Burst Potential and Stability of Rock Mass during Underground Extraction of a Highly Stressed Coal Seam under Massive Strata-a Field Study. *Eng. Geol.* **2023**, *322*, 107178. [CrossRef]
51. Lu, J.; Yin, G.; Gao, H.; Li, X.; Zhang, D.; Deng, B.; Wu, M.; Li, M. True Triaxial Experimental Study of Disturbed Compound Dynamic Disaster in Deep Underground Coal Mine. *Rock Mech. Rock Eng.* **2020**, *53*, 2347–2364. [CrossRef]
52. Zhang, Y.; Okere, C.J.; Su, G. Effect of Loading Rates on Accurate In-Situ Stress Determination in Different Lithologies via Kaiser Effect. *Arab. J. Geosci.* **2021**, *14*, 1304. [CrossRef]
53. Miao, S.J.; Cai, M.F.; Guo, Q.F.; Huang, Z.J. Rock Burst Prediction Based on In-Situ Stress and Energy Accumulation Theory. *Int. J. Rock Mech. Min. Sci.* **2016**, *83*, 86–94. [CrossRef]
54. Jia, Z.; Li, C.; Zhang, R.; Wang, M.; Gao, M.; Zhang, Z.; Zhang, Z.; Ren, L.; Xie, J. Energy Evolution of Coal at Different Depths Under Unloading Conditions. *Rock Mech. Rock Eng.* **2019**, *52*, 4637–4649. [CrossRef]
55. Xu, J.; Jiang, J.; Xu, N.; Liu, Q.; Gao, Y. A New Energy Index for Evaluating the Tendency of Rockburst and Its Engineering Application. *Eng. Geol.* **2017**, *230*, 46–54. [CrossRef]
56. Hao, Q.; Zhang, R.; Gao, M.; Xie, J.; Ren, L.; Zhang, A. Characterization of Energy-Driven Damage Mechanism and Gas Seepage in Coal under Mining-Induced Stress Conditions. *Int. J. Rock Mech. Min. Sci.* **2024**, *181*, 105834. [CrossRef]
57. Cui, F.; Sun, J.; Lai, X.; Jia, C.; Zhang, S. Study on the Energy Release Law of Overburden Rock Breaking and Anti-Rockburst Technology in the Knife Handle Working Face of a Gently Inclined Coal Seam. *Appl. Sci.* **2023**, *13*, 11809. [CrossRef]
58. Yadav, A.; Behera, B.; Sahoo, S.K.; Singh, G.S.P.; Sharma, S.K. Numerical Analysis of the Gob Stress Distribution Using a Modified Elastic Model as the Gob Constitutive Model. *J. Inst. Eng. Ser. D* **2020**, *101*, 127–139. [CrossRef]
59. Zhang, G.; Chen, L.; Wen, Z.; Chen, M.; Tao, G.; Li, Y.; Zuo, H. Squeezing Failure Behavior of Roof-Coal Masses in a Gob-Side Entry Driven under Unstable Overlying Strata. *Energy Sci. Eng.* **2020**, *8*, 2443–2456. [CrossRef]